Elastic stability of CO_2 phase I under high temperature and pressure

Siyang Guo,[1] Xiaoli Huang,[1] Sergey N. Tkachev,[2] Xinpeng Fu,[1] Jung-fu Lin,[3] Xinyang Li,[4] Zhu Mao,[4] Qiang Zhou,[1] Fangfei Li,[1,*] and Tian Cui[1]

[1]*State Key Laboratory of Superhard Materials, College of Physics, Jilin University, Changchun 130012, China*

[2]*Center for Advanced Radiation Sources, University of Chicago, Chicago, Illinois 60637, USA*

[3]*Department of Geological Sciences, the University of Texas at Austin, Austin, Texas 78712, USA*

[4]*Laboratory of Seismology and Physics of Earth's Interior, School of Earth and Space Sciences, University of Science and Technology of China, Hefei, Anhui 230026, China*

(Received 6 June 2018; published 15 October 2018)

Carbon dioxide exhibits a richness of high-pressure polymorphs ranging from typical molecular solids to fully extended covalent solids, which, in turn, makes it a very appealing topic of fundamental research in condensed-matter physics and simultaneously provides valuable insights into the routes of developing possibly novel materials with advanced properties. The single-crystal x-ray diffraction (XRD) and Brillouin scattering spectroscopy of CO_2-I were performed under high temperature and pressure. Densities, acoustic velocities, and elastic moduli of CO_2-I were obtained along 300-, 400-, and 580-K isotherms up to the phase-transition boundaries. CO_2-I transforms to phase III and phase IV at room temperature (at 12.19 GPa) and 580 K (at 10.83 GPa), respectively. It was observed that high temperature suppresses pressure-induced stress in single-crystal CO_2-I. All elastic constants and thermal elasticity parameters of CO_2-I were obtained and analyzed using finite-strain theory and thermal equation of state modeling. The C_{11}, C_{12}, and K_S increase almost linearly with pressure, while shear moduli C_{44} and G exhibit a downward trend with pressure, showing a noticeable reduction at higher temperature. Elastic anisotropy A is practically independent of pressure along each isotherm and increases from 1.75 to 1.9.

DOI: 10.1103/PhysRevB.98.134107

I. INTRODUCTION

Carbon dioxide as a simple molecule, besides being abundant in nature and commonly found on Earth and other outer solar planetary bodies, provides unique fundamental constraints on possible routes for development of novel materials with advanced properties via investigation of its basic thermodynamic characteristics under extreme conditions. The phase structure and boundary exploration on CO_2 has been conducted over decades from both experimental and theoretical standpoints of chemical physics [1–11]. CO_2 molecule is linear symmetric with a large quadrupole moment at ambient conditions [12]. It turns into a molecular CO_2-I solid (dry ice with a cubic structure Pa-3) [13–15], which consists of both strong covalent intramolecular bond and relatively weak quadrupole interactions between molecules and is stable below 12 GPa, when decreasing temperature or increasing pressure. Above that pressure CO_2-I transforms into phase IV (rhombohedral, $R\bar{3}c$) [16,17], associated phase II ($P4_2/mnm$), and strained phase III (orthorhombic, $Cmca$) depending on the transition temperature [18,19]. A further compression of CO_2 results in the appearance of extended solid phases consisting of monolithic 3D covalently bonded network structures, such as fourfold CO_2-V [9,20], pseudosixfold CO_2-VI [4,21,22], coesitelike CO_2 (c-CO_2), and amorphous a-carbonia (a-CO_2) [3,21].

There is a large number of polymorphs of CO_2 under high temperature and pressure. The structural stability of various CO_2 phases and transitions among them were widely discussed both in theory and experiments. CO_2-I, or dry ice, is regarded as stable below 12 GPa. The transformation to a molecular CO_2-III solid has been confirmed by x-ray diffraction (XRD) studies [1,19] at temperatures below 400 K. Raman measurements have also indicated that the CO_2 I-III transition occurs at 12 GPa and 400 K [23]. Shieh *et al.* have recently investigated the local electronic structure of CO_2-I using x-ray Raman spectroscopy and observed the subtle variations of the oxygen K-edge spectra, which show the CO_2-III features at around 7 GPa [24], thus, shedding new light on the stability field of phase I. Zhang *et al.* have also performed a single-crystal elasticity study of CO_2 across the I-III transition and noticed a decrease in anisotropy above 8 GPa, which is possibly resulting from a subtle structural change [25].

CO_2-I transforms into phase VII, phase IV, or phase II (even though latter ones can be quenched to room temperature [23,26], phase II is considered to be more stable than phase III at room temperature [24]) above 400 K [10]. However, the exact nature of phase transition is complicated and not well known, due to large lattice strains, phase metastabilities, and strong kinetics. On the other hand, single-crystal elasticity is expected to be highly sensitive to any structural changes and might, therefore, provide valuable insights into the physics of CO_2 phase transitions. Brillouin scattering spectroscopy is a powerful method of choice to investigate the single-crystal

*Corresponding author: lifangfei@jlu.edu.cn

elastic property changes, and it has been already successfully used by Zhang *et al.* and Shimizu *et al.* to report the room-temperature elasticity of CO_2-I up to 6 and 11.7 GPa, respectively [25,27]. Moreover, Giordano *et al.* were the first to carry out the high-temperature Brillouin study of liquid and supercritical CO_2, that resulted in determination of the melting curve and the fluid equation of state (EOS) [28], as well as an XRD and spectroscopic investigation of CO_2-I, extending the EOS up to 12 GPa and 800 K [29]. In this study, we present an *in situ* single-crystal Brillouin scattering and XRD measurements of CO_2-I at simultaneously high temperature and pressure, up to 10.83 GPa and 580 K. The acoustic velocities, densities, and elastic constants along with the elastic anisotropies were determined and discussed.

II. METHODS

The present experiments were conducted with a BX90 externally heated diamond-anvil cell (EHDAC) with a symmetrical 90° axial opening [30], which allows both Brillouin scattering and single-crystal XRD studies. Preindented rhenium plate with a thickness of about 40 μm was used as a gasket. A ruby chip was placed in the sample chamber for pressure calculation. The high-purity CO_2 samples were loaded in the sample chamber using the GSECARS/COMPRES gas-loading system at room temperature [31]. Pressure was determined from the ruby scale [32,33] with an uncertainty of about 0.05 GPa at 580 K. The EHDAC was heated by a miniature resistive heater, which was made of coiled 200-μm-thick Pt wires and mounted around the diamonds and the gasket. The temperature of the sample chamber was monitored using a *K*-type thermocouple attached to one of the diamond anvils, approximately 500 μm away from the diamond culet.

The angular dispersive XRD measurements were performed on 13-BMD beamline, GSECARS of the Advanced Photon Source (APS), Argonne National Laboratory, to verify the single-crystal state and calculate the density of the sample under high temperature and high pressure (HTHP). The wavelength of monochromatic x-ray beam was 0.3344 Å with a focused beam spot size of 5 × 15 μm. The 2D diffraction patterns were recorded on a PerkinElmer detector. Brillouin scattering spectra of CO_2-I at HTHP were collected using a six-pass tandem Fabry-Perot interferometer (JRS Scientific) integrated in 13-BMD beamline. The scattered light from a solid-state diode-pumped laser (532-nm) excitation was collected in 50° symmetric scattering geometry [34]. The diamond-anvil cell (DAC), which was fixed on a rotation-translation stage prealigned with the x-ray beam, can be rotated around both the axis perpendicular to the incident x-ray beam for diffraction data collection to map the reciprocal lattice and the optical axis of the DAC for Brillouin spectra collection on one crystal plane. We used a rotation range of 30° around the vertical axis for diffraction measurements and a rotation step of 10° for Brillouin measurements in this study. An online ruby system was utilized to conduct *in situ* both visual monitoring the sample and collecting the ruby fluorescence signal.

The pressure was gradually and repeatedly fluctuated around the melting (if the pressure was decreasing) and crystallization (if the pressure was increasing) pressures, in order to grow a CO_2 single crystal in the sample chamber at room temperature (Fig. 1). Room-temperature (300-K isotherm) sound-velocity measurements were performed using a Brillouin scattering spectroscopy setup at Jilin University [35]. Two HTHP experimental runs (400- and 580-K isotherms shown in Fig. 2) were conducted at GSECARS within a two-year period. Brillouin spectra were collected at each pressure, after the XRD pattern was measured.

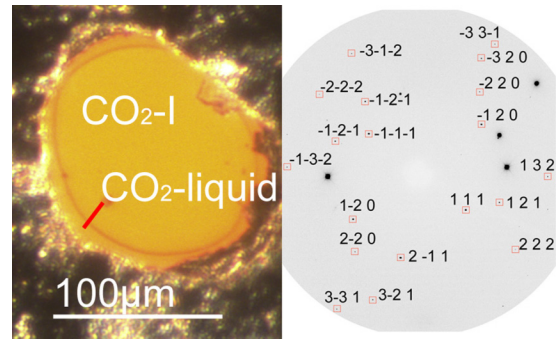

FIG. 1. (Left) A single crystal of CO_2 in coexistence with liquid CO_2 at room temperature. (Right) XRD pattern of the CO_2-I single crystal at 6.6 GPa and room temperature. The CO_2-I diffraction spots are indicated by open red squares with the corresponding *hkl* indices. The broad intense XRD spots are from the diamonds. Because of the hydrostatic conditions in the sample chamber, the CO_2-I reflections have round shape.

III. RESULTS AND DISCUSSION

A. CO_2 single-crystal x-ray diffraction

When a CO_2 single crystal grows in the liquid at 300 K, it is a nearly perfect crystal without any residual stress. When the pressure in the sample chamber is increased, the coexistence of the single crystal with liquid CO_2 will eventually disappear, resulting in an almost instantaneous emergence (and subsequent growth) of the internal stress in the solid, which will completely fill up the sample chamber by that time, and it will not take long when a small amount of phase III will (Fig. 3) appear at the edge of the gasket at 12.19 GPa. When

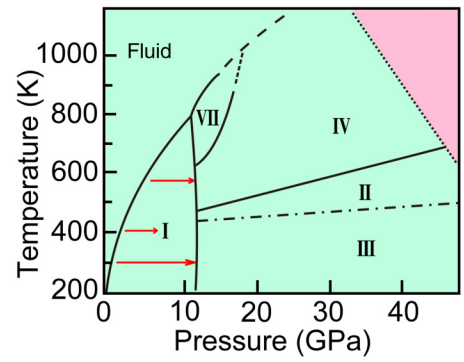

FIG. 2. Phase diagram of CO_2. The *P*-*T* conditions investigated in this study are marked by red arrows. Brillouin spectra were collected along the isotherms during compression cycle. This previously published [4] and subsequently modified [17] figure is adapted for the purposes of the demonstration.

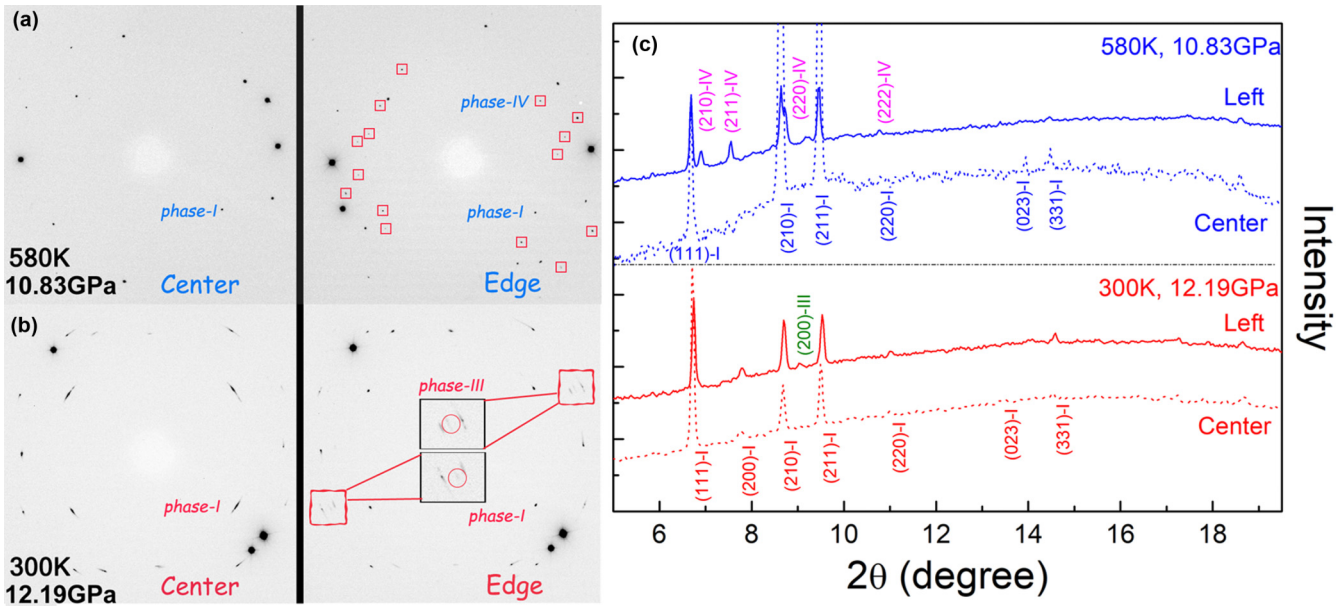

FIG. 3. Diffraction images of CO_2 at (a) 10.83 GPa and 580 K and at (b) 12.19 GPa and 300 K. CO_2-IV reflections are marked by red squares in (a). Four diffraction spots near the center become less elongated in a phase I and III mixture, when a weak (200) reflection from CO_2-III, which emerges at the edge of the sample chamber, appears in (b). (c) Integrated XRD patterns of CO_2 (580 K: blue solid and dotted lines represent the XRD patterns taken at the edge of and in the center of the sample chamber, respectively; 300 K: red solid and dotted lines represent the XRD patterns taken at the edge of and in the center of the sample chamber, respectively) at HTHP. Reflections from CO_2-IV are marked with *hkl* indices. A weak reflection from CO_2-III (200) crystal face is labeled.

the pressure exceeds 12.19 GPa, phase III will be observed in the center of the sample chamber, as well.

The increased stress in the single crystal of CO_2 along the 300-K isotherm is also visible in the 2D diffraction images, where the initially round diffraction spots become elongated at higher pressure. The internal stress is effectively released when the temperature is increased. All diffraction patterns along the 580-K isotherm [Fig. 3(a)] demonstrate the perfect round diffraction spots even at the phase I–IV boundary pressure. Although phase IV is not optically observable in the stress-free sample at 580 K and 10.83 GPa, the XRD reveals the presence of phase IV near the edge of the sample chamber, whereas phase I still remains in the center. The CO_2-I single crystal fractures into a few pieces and transforms into CO_2-IV upon further compression.

It is obvious that in this study *P-T* conditions of the phase transitions agree well with the existing CO_2 phase diagram (Fig. 2). Since the poor optical quality of phases III and IV was not conducive to obtaining any Brillouin spectra with high signal-to-noise ratio from those phases, the *in situ* HTHP XRD measurements were carried out to confirm and monitor the presence of the CO_2-I single crystal, from which the Brillouin spectra were then collected. Noteworthy, the pressure-induced stress in phase I is released (Fig. 3) as soon as the coexistence between phases I and III occurs.

B. CO_2 single-crystal Brillouin scattering and thermoelastic modeling

In this study, the Brillouin spectra were measured along isotherms upon compression. To calculate the velocity (v) from Brillouin spectra in a symmetric scattering geometry, the following equation, which does not require the information on the refractive index of the sample, can be used:

$$\mathrm{v} = \Delta\nu^{*}\lambda/2\sin(\theta/2), \tag{1}$$

where $\Delta\nu$ is the frequency shift obtained by averaging the Stokes and anti-Stokes modes in Brillouin spectra, λ is the wavelength of incident laser beam, and θ is the scattering angle. In order to determine the density (ρ) of the sample and confirm that it is still in phase I, the XRD patterns of CO_2 were also collected at each given *P-T* for 400- and 580-K isotherms. Since there are available literature density data of CO_2 [30], it was not necessary to perform XRD for the elastic moduli to be calculated along the 300-K isotherm. All Brillouin spectra are of good quality with high signal-to-noise ratios (Fig. 4).

The crystal was rotated around the optical axis of the DAC, and the sound velocities were measured every 10° from 0° to 180° range (Fig. 5) at each *P-T* point. The single-crystal elastic moduli (*Cij*) can be obtained from the angular dependence of the acoustic velocities and crystal orientation of CO_2-I using the Christoffel equation [36]:

$$|C_{ijkl}\mathrm{n}_i\mathrm{n}_j - \rho\mathrm{v}^2\delta_{ik}| = 0, \tag{2}$$

where v is the measured velocity, ρ is the density, and δ_{ik} is the Kronecker delta function. The single-crystal elastic constants, C_{ijkl}, are written in a full suffix notation in the equation, although reduced Voigt notation, C_{ij}, has been utilized for the reported values. $\mathrm{n_i}$ represents the direction cosine of the phonon propagation direction, which can be described by three Eulerian angles (θ, χ, φ) and determined by carrying out the single-crystal XRD measurements. A final root-mean-square error in a least-square best fitting for the

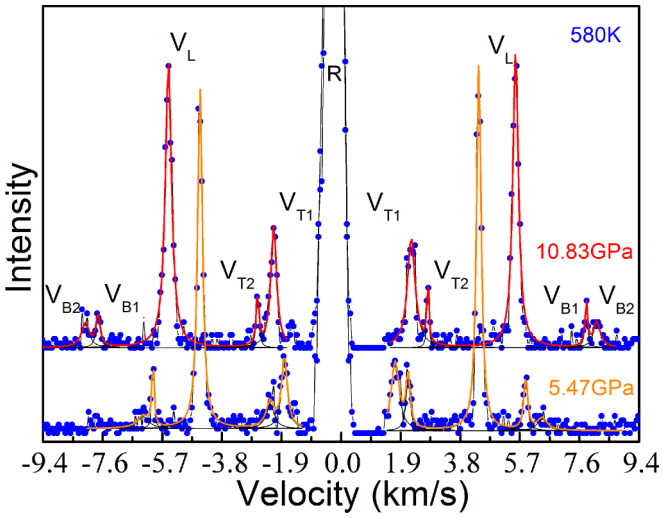

FIG. 4. Brillouin spectra of CO_2-I single crystal at 5.47 GPa and 10.83 GPa at 580 K. R indicates the elastic Rayleigh peak, V_{T1} and V_{T2} indicate two transverse waves and V_L is the longitudinal wave. V_{B1} and V_{B2} come from a weak backscattering of the incident laser beam reflected by the diamond culet.

three independent C_{ij} (solid and dotted lines in Fig. 5) is within 0.05 km/s even at the highest pressure and 580 K.

There are a total of three independent elastic constants, C_{11}, C_{12}, and C_{44}, for cubic CO_2-I. The longitudinal and off-diagonal moduli follow a nearly linear increase with pressure, whereas the shear moduli, C_{44}, exhibit a downward trend toward higher pressures along the 300-, 400-, and 580-K isotherms (Fig. 6). The adiabatic bulk modulus, $K_s = (C_{11} + 2^*C_{12})/3$, and the Voigt-Reuss-Hill averaged shear modulus, $G = (G_V + G_R)/2$, where G_V is the effective Voigt shear modulus and G_R is the Reuss shear modulus, can be obtained using the following equations [37]:

$$G_V = [(2^*C') + (3^*C)]/5,\ G_R = 15/[(6/C') + (9/C)], \tag{3}$$

and

$$C = C_{44},\quad C' = (C_{11} - C_{12})/2. \tag{4}$$

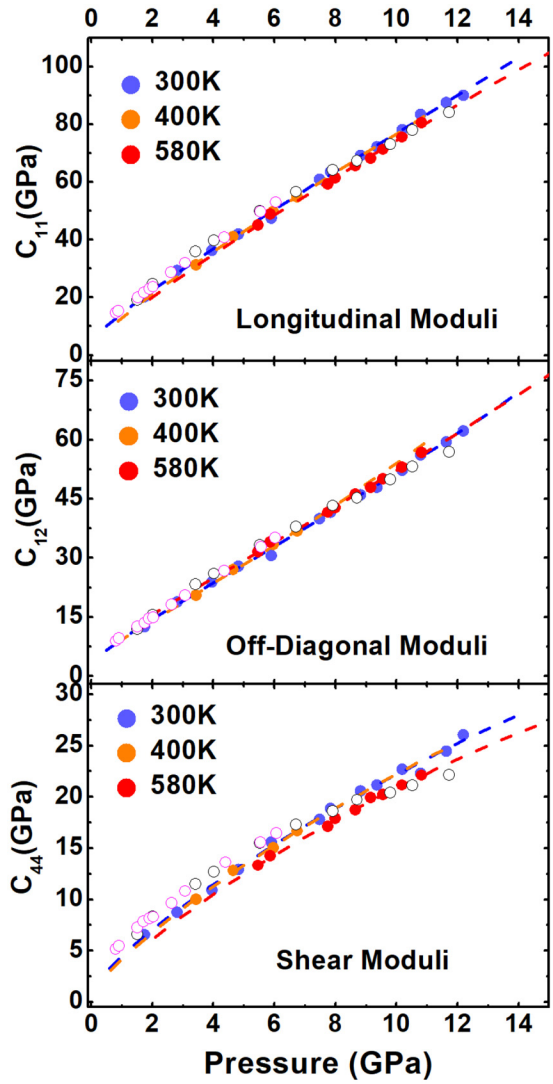

FIG. 6. Elastic moduli of CO_2-I single crystal at high *P*-*T*. Symbols are color-coded for each isotherm. The uncertainties are within the symbols. Solid circles: this study; open circles: Shimizu *et al.* [27] (pink), Zhang *et al.* [25] (black).

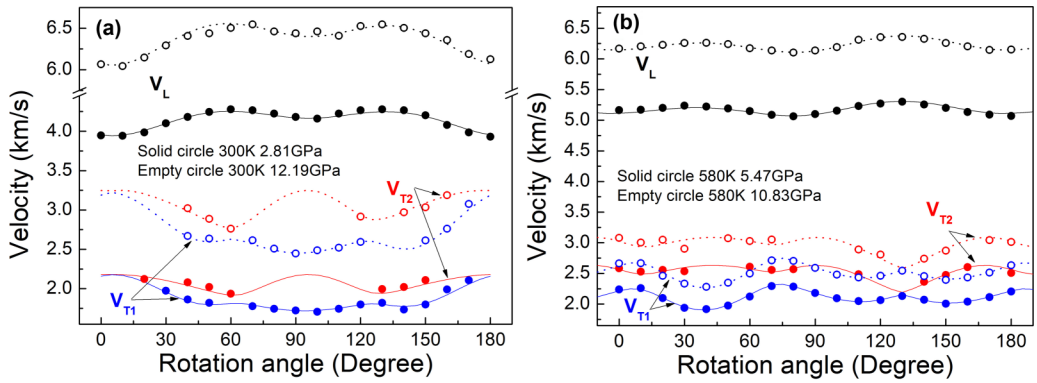

FIG. 5. Sound velocity variations vs rotation angle in one crystal plane at 300 and 580 K. (a) Solid symbols are the sound velocities measured at 2.81 GPa and 300 K, the empty symbols are the sound velocities measured at 12.19 GPa and 300 K. (b) Solid symbols are the sound velocities measured at 5.47 GPa and 580 K, the empty symbols are the sound velocities measured at 10.83 GPa and 580 K. Solid and dotted lines are the sound velocities calculated from the best-fit elastic constants. The velocity uncertainties are within the symbols.

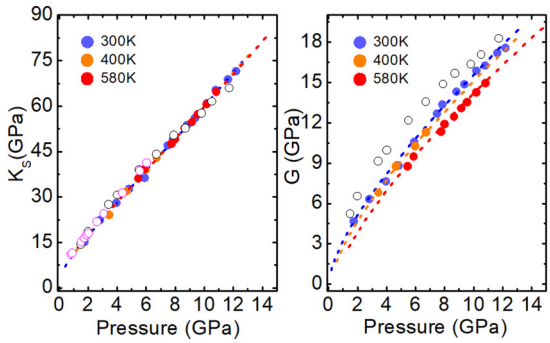

FIG. 7. Aggregate elastic moduli of CO_2-I single crystal at HTHP. Symbols are color-coded for each isotherm. The uncertainties are within the symbols. Solid circles: this study; open circles: Shimizu *et al.* [27] (pink), Zhang *et al.* [25] (black).

Although K_S increases almost linearly with pressure, G exhibits a downward trend with pressure (Fig. 7, Table I), due to the softening of the shear moduli C_{44} (Fig. 6). The adiabatic elastic constants, C_{ij0}, adiabatic bulk and shear modulus, K_{S0} and G_0, at ambient conditions, as well as their P-T derivatives can be obtained (Table II) by fitting the moduli at high pressure using the fourth-order Eulerian finite-strain equation [38] (as listed below):

$$C_{ij0}(T) = C_{ij0}(300\,\mathrm{K}) + (T - 300)(\partial C_{ij}/\partial T)_P, \quad (5)$$

TABLE II. Elastic moduli of CO_2 single crystal at ambient pressure as a function of experimental temperatures.

	K_{S0} (GPa)	G_0 (GPa)	C_{11} (GPa)	C_{12} (GPa)	C_{44} (GPa)
300 K	3.16(5)	0.32(7)	4.58(1)	3.23(9)	1.04(7)
400 K	3.13(5)	−0.13(3)	2.73(2)	3.65(1)	0.68(4)
580 K	3.08(1)	−0.97(5)	1.50(6)	4.39(3)	0.03(1)

$$C_{ij} = (1 + 2f)^{7/2}[C_{ij0}(T) + a_1 f + a_2 f^2] + a_3 P, \quad (6)$$

$$a_1 = 3KT_0(C'_{ij}-3) - 7C_{ij0}(T), \quad (7)$$

$$a_2 = 9K^2{}_T0(T)C''_{ij} + K_{T0}(T)(9K'_{T0} - 48)(C'_{ij} - 3) + 63C_{ij0}(T), \quad (8)$$

$$f = (1/2)[(V_0/V)^{2/3}-1], \quad (9)$$

where f is the Eulerian strain, V_0 and V are the unit-cell volumes at ambient condition and high pressures, C_{ij0} (300 K) is the derived zero-pressure constant from ambient measurements and is thus fixed for the modeling, C_{ij0} (T) is the elastic constant at high temperatures and 1 bar, $C'_{ij} = (\partial C_{ij}/\partial P)_T$ is the pressure derivative of the elastic constants, $C''_{ij} = (\partial^2 C_{ij}/\partial^2 P)_T$ is the second pressure derivative of the elastic constants.

TABLE I. Elastic constants of CO_2-I as functions of the sample density. Numbers in parentheses are standard deviations.

T, K	ρ, g/cm^3	P, GPa	C_{11}, GPa	C_{12}, GPa	C_{44}, GPa	K_S, GPa	G_S, GPa	A	Cauchy relation
300	1.777	1.74	20.27(7)	12.58(7)	6.591	15.15(0)	4.66(9)	1.714	2.51
	1.887	2.81	29.38(2)	18.84(3)	8.77(5)	22.35(6)	6.32(1)	1.665	4.448
	1.984	3.95	36.35(9)	23.91(9)	10.94(1)	28.06(5)	7.63(6)	1.759	5.078
	2.049	4.82	42.00(6)	27.94(8)	12.95(3)	32.63(4)	8.80(6)	1.843	5.355
	2.122	5.90	47.51(3)	30.68(1)	15.61(3)	36.29(2)	10.57(5)	1.855	3.267
	2.219	7.48	60.95(8)	40.01(7)	17.82(1)	46.99(7)	12.67(6)	1.702	7.236
	2.240	7.84	63.61(1)	41.63(4)	18.88(5)	48.95(9)	13.35(8)	1.719	7.069
	2.295	8.82	69.25(0)	46.02(9)	20.60(6)	53.76(9)	14.30(9)	1.775	7.783
	2.324	9.36	72.27(2)	47.95(9)	21.17(1)	56.06(3)	14.86(1)	1.741	8.068
	2.368	10.19	78.18(7)	52.31(0)	22.71(1)	60.93(6)	15.87(0)	1.755	9.219
	2.399	10.79	83.47(9)	56.18(1)	22.31(7)	65.28(0)	16.24(9)	1.635	12.284
	2.441	11.63	87.61(7)	59.47(4)	24.47(8)	68.85(5)	17.19(3)	1.740	11.736
	2.469	12.19	90.07(6)	62.25(2)	26.08(0)	71.52(3)	17.56(4)	1.875	11.792
400	1.907	3.45	31.30(7)	20.49(4)	10.01(9)	24.09(8)	6.79(0)	1.853	3.575
	1.998	4.66	41.13(2)	27.07(9)	12.80(1)	31.76(3)	8.75(9)	1.822	4.966
	2.085	5.97	49.82(8)	33.44(8)	15.03(6)	38.90(8)	10.24(4)	1.836	6.468
	2.132	6.75	54.79(0)	36.82(4)	16.65(8)	42.81(3)	11.28(5)	1.854	6.672
580	2.033	5.47	45.10(3)	31.56(5)	13.32(5)	36.07(7)	8.73(6)	1.968	7.294
	2.058	5.87	48.89(6)	34.02(9)	14.26(3)	38.98(5)	9.48(2)	1.919	8.014
	2.165	7.76	59.22(3)	41.56(1)	17.10(5)	47.44(8)	11.31(3)	1.937	8.938
	2.178	8.01	61.38(5)	42.74(7)	17.89(0)	48.95(9)	11.89(0)	1.920	8.847
	2.212	8.66	65.63(3)	46.12(0)	18.72(8)	52.62(4)	12.44(8)	1.920	10.062
	2.237	9.18	68.13(9)	47.84(0)	19.89(5)	54.60(5)	13.07(3)	1.960	9.613
	2.256	9.56	71.30(7)	50.05(1)	20.23(5)	57.13(6)	13.51(0)	1.904	10.706
	2.286	10.18	75.56(4)	53.01(3)	21.15(2)	60.52(9)	14.23(8)	1.876	11.491
	2.316	10.83	80.53(1)	56.80(4)	22.10(2)	64.71(3)	14.93(5)	1.863	13.038

TABLE III. Comparison of the elastic moduli at ambient conditions.

	Pressure	K_{S0} (GPa)	G_0 (GPa)	C_{11} (GPa)	C_{12} (GPa)	C_{44} (GPa)
This study	12.19	3.16(5)	0.32(7)	4.58(1)	3.23(9)	1.04(7)
Zhang *et al.* (2014) [25]	11.73	3.4(6)	1.8(2)	5.3(8)	2.5(5)	2.3(2)
Shimizu *et al.* (1993) [27]	6	5.82	1.22	7.54	4.98	2.25
Giordano *et al.* (2010) [29]	12	3				

Even though the shear modulus obtained in this study is much smaller than that from previous works [26,28], in which the discrepancy in G_0 may be caused by the use of different fitting functions, the adiabatic bulk moduli agree well at 300 K (Table II and Table III), with the exception of $K_{S0} = 5.82$ GPa [28]. Interestingly, as temperature is elevated at a given pressure, the bulk modulus variation is very small and comparable to that of C_{11} and C_{12}, whereas the temperature-induced reduction of shear modulus is more pronounced.

$K_{T0}(T)$, which is the isothermal bulk modulus at 1 bar and high temperature, and $K'_{T0} = (\partial K_{T0}/\partial P)_T$, which is the pressure derivative of the bulk modulus, are calculated from the adiabatic bulk modulus K_{S0} and K'_{S0} as follows:

$$K_{T0}(300\,\mathrm{K}) = K_{S0}/(1+\alpha\gamma T), \tag{10}$$

$$K_{T0}(T) = K_{T0}(300\,\mathrm{K}) + (\partial K_T/\partial T)_P(T-300), \tag{11}$$

$$K'_{T0} = (1+\alpha\gamma T)^{-1}[K'_{S0} - \gamma T/K_{T0}(T)(\partial K_T/\partial T)_P], \tag{12}$$

$$(\partial K_T/\partial T)_P = (\partial K_S/\partial T)_P/(1+\alpha\gamma T) - K_S(T)/(1+\alpha\gamma T)^2 \times [\alpha\gamma + (\partial\alpha/\partial T)\gamma T], \tag{13}$$

where $a_3 = 3$ for C_{11}, C_{22}, and C_{33}, and $a_3 = 1$ for all other elastic moduli. $K'_{S0} = 12.35(3)$ and $K''_{S0} = -31.51(5)$ have been obtained by fitting K_S at high pressures and 300 K with the fourth finite equation and a fixed $K_{S0} = 3.16(5)$ GPa as well as a literature value of 5.015 for Grüneisen parameter γ [30] in a self-consistent density model. Furthermore, the values of $-0.298(8)$ MPa/K and $5.36 \times 10^{-4}\,\mathrm{K}^{-1}$ have, thus, also been possible to determine with K'_{S0} and high P-T K_S results for the temperature derivative of the bulk modulus, $(\partial K_S/\partial T)_P$, and thermal expansion coefficient at ambient conditions, respectively.

The P-T derivatives of the shear modulus (Table IV) were evaluated using the following equations:

$$G_0(T) = G_0(300\,\mathrm{K}) + (\partial G/\partial T)_P(T-300), \tag{14}$$

$$G = (1+2f)^{5/2}[G_0(T) + b_1 f + 1/2 b_2 f^2], \tag{15}$$

$$b_1 = 3K_{T0}(T)G'_0 - 5G_0(T), \tag{16}$$

$$b_2 = 9\{K^2{}_{T0}(T)[G''_0 + 1/K_{T0}(T)(K'{}_{T0}-4)G'_0] + 35G_0(T)/9\}. \tag{17}$$

In general, the shear moduli C_{44} and G pressure dependence adheres to a well-known pattern [39–41] of the elastic constants behavior under pressure approaching phase transition. Nevertheless, even though CO_2-I transforms to phase III at 300 K and phase IV at 580 K, its sound velocities do not quite follow the trend characteristic for the onset of shear instability, and, therefore, it is reasonable to assume that the internal stress plays a more defining role in what pressure-induced phase structure of CO_2 will be favorable to at certain temperature. This assertion can also be circumstantially supported by the fact that every time there is an occurrence of a coexistence between two phases of CO_2 in the sample chamber upon compression, the XRD demonstrates the stress release in the precursor phase.

Elastic anisotropy (A) for cubic crystals is defined as $A = (V_{T2}/V_{T1})^2 = 2C44/(C11-C12)$, where the V_{T2} and V_{T1} are sound velocities of two transverse waves propagating along ⟨110⟩ direction, and, if two transverse velocities are equal, then $A = 1$ for isotropic elasticity. A for orientationally ordered CO_2-I (Fig. 8) is around 1.75, which is close to MgO's $A = 1.36$ at ambient pressure, and practically independent of pressure, which is a typical behavior of most solids. However, as a molecular solid, CO_2-I possesses a much smaller A value than the molecular solids characterized by a molecular rota-

TABLE IV. Temperature and pressure derivatives of the elastic moduli for CO_2 single crystal.

$(\partial K_S/\partial T)_P$ (MPa/K)	$(\partial G/\partial T)_P$ (MPa/K)	$(\partial C_{11}/\partial T)_P$ (MPa/K)	$(\partial C_{12}/\partial T)_P$ (MPa/K)	$(\partial C_{44}/\partial T)_P$ (MPa/K)
−0.298(8)	−5.00(7)	−6.80(1)	4.11(9)	−3.63(4)
$(\partial K_S/\partial P)_T$	$(\partial G/\partial P)_T$	$(\partial C_{11}/\partial P)_T$	$(\partial C_{12}/\partial P)_T$	$(\partial C_{44}/\partial P)_T$
12.35(3)	4.87(6)	22.94(1)	15.20(3)	8.34(9)
$(\partial^2 K_S/\partial P^2)_T$ (1/GPa)	$(\partial^2 G/\partial P^2)_T$ (1/GPa)	$(\partial^2 C_{11}/\partial P^2)_T$ (1/GPa)	$(\partial^2 C_{12}/\partial P^2)_T$ (1/GPa)	$(\partial^2 C_{44}/\partial P^2)_T$ (1/GPa)
−31.51(5)	−14.21(1)	−41.56(1)	−24.43(2)	−17.48(3)

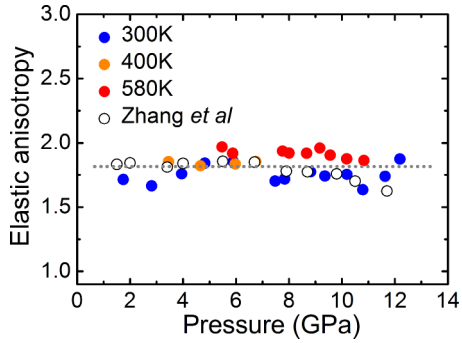

FIG. 8. Pressure dependence of elastic anisotropy for CO_2-I along the 300-, 400-, and 580-K isotherms. The uncertainties are within the symbols.

tion in an orientationally disordered cubic phase, such as H_2S ($A \cong 3.5$), NH_3 ($A \cong 4$), and CH_4($A \cong 5$) and so on, because the rotation-translation coupling of molecular motions may increase the elastic anisotropy [42]. The anisotropy slightly increases to $A = 1.9$, due to a possible temperature-induced gradual increase of space for presumably larger variations of anisotropy, at higher temperatures, but still remains practically independent of pressure changes (Fig. 8).

The high-pressure Cauchy relation $C_{12}-C_{44} = 2P$ will be satisfied for cubic crystals under hydrostatic conditions when interatomic forces are purely central [43]. The deviations from the Cauchy condition $(C_{12}-C_{44})-2P$ measured in this study (Table I) indicate the presence of noncentral forces in CO_2-I. These deviations increase with pressure along all isotherms, suggesting that the noncentral nature of the bonding becomes greater at high pressures. It means that an accurate description of HTHP CO_2 requires careful consideration of many-body interactions. Moreover, it is known that the temperature effect on Cauchy condition is small for solid Ar (<1% for Ar above 6 GPa) [44]; in the HTHP CO_2, however, we noticed that the Cauchy relation along the 580-K isotherm becomes about 20% higher than the one along the 300-K isotherm (Table I). This pronounced increase means that theoretical calculations have to be modified to reflect this change when describing the nature of HTHP CO_2.

IV. CONCLUSIONS

Systematic studies of the elastic properties in CO_2-I have been conducted under high pressures along the 300, 400, and 580 K isotherms via Brillouin scattering spectroscopy and XRD measurements. In order to determine the angular dependencies of sound velocities the Brillouin scattering spectra were collected from exactly the same spots where the single-crystal XRD patterns of the sample had been obtained to confirm the presence of phase I. Even though CO_2-I transforms to phase III at 12.19 GPa and 300 K and phase IV at 10.83 GPa and 580 K, the elastic moduli, with the exception of the shear ones, exhibit practically identical pressure dependencies along different isotherms, i.e., longitudinal modulus C_{11}, off-diagonal modulus C_{12}, and bulk modulus K_S increase almost linearly with pressure, whereas C_{44} and G are marked by both a distinct downward deflection from the linear pressure dependence and a visible temperature-induced reduction. Although the limits of the current studies do not allow reaching a more qualitative conclusion with respect to influence of the internal stress on the outcome of the phase transitions in the single crystal of CO_2, the evidence in support of such an influence have been presented and discussed. It has been shown that, in contrast to other molecular solids, CO_2-I has a relatively low (around 1.75 at room temperature and 1.9 at 580 K) elastic anisotropy A. In addition, the violation of the Cauchy relation with pressure suggests that the noncentral nature of the bonding in CO_2-I becomes greater at high pressures. These experimental results on acoustic velocities, adiabatic elastic moduli, their temperature and pressure derivatives, and elastic anisotropies provide valuable data for high-pressure science and for deciphering CO_2's properties at extreme conditions.

ACKNOWLEDGMENTS

This work was supported by the National Key Research and Development Program (No. 2017YFA0403704), the National Natural Science Foundation of China (Grants No. 11474127, No. 11574112, No. 11274137, and No. 11504127), Program for Changjiang Scholars and Innovative Research Team in University (Grant No. IRT_15R23), National Foundation for Fostering Talents of Basic Science (Grant No. J1103202). Portions of this work were performed at GeoSoilEnviroCARS (The University of Chicago, Sector 13), Advanced Photon Source (APS), Argonne National Laboratory. GeoSoilEnviroCARS is supported by the National Science Foundation - Earth Sciences (Grant No. EAR - 1634415) and Department of Energy- GeoSciences (Grant No. DE-FG02-94ER14466). This research used resources of the APS, a US Department of Energy (DOE) Office of Science User Facility operated for the DOE Office of Science by Argonne National Laboratory under Contract No. DE-AC02-06CH11357.

[1] C.-S. Yoo, Phys. Chem. Chem. Phys. **15**, 7949 (2013).
[2] C.-S. Yoo, A. Sengupta, and M. Kim, Angew. Chem. Int. Ed. **50**, 11219 (2011).
[3] M. Santoro, F. A. Gorelli, R. Bini, G. Ruocco, S. Scandolo, and W. A. Crichton, Nature (London) **441**, 857 (2006).
[4] V. Iota, C.-S. Yoo, K. Jae-Hyun, Z. Jenei, and W. Evans, Nat. Mater. **6**, 34 (2007).
[5] T. Kume, Y. Ohya, M. Nagata, S. Sasaki, and H. Shimizu, J. Appl. Phys. **102**, 53501 (2007).
[6] J.-H. Park, C. S. Yoo, V. Iota, H. Cynn, M. F. Nicol, and T. Le Bihan, Phys. Rev. B **68**, 014107 (2003).
[7] M. Santoro, J.-F. Lin, H.-K. Mao, and R. J. Hemley, J. Chem. Phys. **121**, 2780 (2004).
[8] M. Santoro and F. A. Gorelli, Chem. Soc. Rev. **35**, 918 (2006).

[9] V. Iota, C.-S. Yoo, and H. Cynn, Science **283**, 1510 (1999).
[10] S. A. Bonev, F. Gygi, T. Ogitsu, and G. Galli, Phys. Rev. Lett. **91**, 065501 (2003).
[11] B. Holm, R. Ahuja, A. Belonoshko, and B. Johansson, Phys. Rev. Lett. **85**, 1258 (2000).
[12] M. R. Battaglia, A. D. Buckingham, D. Neumark, R. K. Pierens, and J. H. William, Mol. Phys. **43**, 1015 (1981).
[13] P. W. Bridgeman, Proc. Am. Acad. Arts Sci. **72**, 207 (1938).
[14] R. C. Hanson and L. H. Jones, J. Chem. Phys. **75**, 1102 (1981).
[15] B. Olinger, J. Chem. Phys. **77**, 6255 (1982).
[16] F. A. Gorelli, V. M. Giordano, P. R. Salvi, and R. Bini, Phys. Rev. Lett. **93**, 205503 (2004).
[17] F. Datchi, V. M. Giordano, P. Munsch, and A. M. Saitta, Phys. Rev. Lett. **103**, 185701 (2009).
[18] C.-S. Yoo, H. Kohlmann, H. Cynn, M. F. Nicol, V. Iota, and T. LeBihan, Phys. Rev. B **65**, 104103 (2002).
[19] K. Aoki, H. Yamawaki, M. Sakashita, Y. Gotoh, and K. Takemura, Science **263**, 356 (1994).
[20] S. Serra, C. Cavazzoni, G. L. Chiarotti, S. Scandolo, and E. Tosatti, Science **284**, 788 (1999).
[21] J. Sun, D. D. Klug, R. Mortonak, J. A. Montoya, M. S. Lee, S. Scandolo, and E. Tosatti, Proc. Natl. Acad. Sci. U.S.A. **106**, 6077 (2009).
[22] J. A. Montoya, R. Rousseau, M. Santoro, F. Gorelli, and S. Scandolo, Phys. Rev. Lett. **100**, 163002 (2008).
[23] V. Iota and C. S. Yoo, Phys. Rev. Lett. **86**, 5922 (2001).
[24] S. R. Shieh, I. Jarrige, M. Wu, N. Hiraoka, J. S. Tse, Z. Mi, L. Kaci, and Y. Q. Cai, Proc. Natl. Acad. Sci. U.S.A. **110**, 18402 (2013).
[25] J. S. Zhang, S. R. Shieh, J. D. Bass, P. Dera, and V. Prakapenka, Appl. Phys. Lett. **104**, 141901 (2014).
[26] C. S. Yoo, V. Iota, and H. Cynn, Phys. Rev. Lett. **86**, 444 (2001).
[27] H. Shimizu, T. Kitagawa, and S. Sasaki, Phys. Rev. B **47**, 11567 (1993).
[28] V. M. Giordano, F. Datchi, and A. Dewaele, J. Chem. Phys. **125**, 054504 (2006).
[29] V. M. Giordano, F. Datchi, F. A. Gorelli, and R. Bini, J. Chem. Phys. **133**, 144501 (2010).
[30] I. Kantor, V. Prakapenka, A. Kantor, P. Dera, A. Kurnosov, S. Sinogeikin, N. Dubrovinskaia, and L. Dubrovinsky, Rev. Sci. Instrum. **83**, 125102 (2012).
[31] M. Rivers, V. B. Prakapenka, A. Kubo, C. Pullins, C. M. Holl, and S. D. Jacobsen, High Press. Res. **28**, 273 (2008).
[32] A. Dewaele, M. Torrent, P. Loubeyre, and M. Mezouar, Phys. Rev. B **78**, 104102 (2008).
[33] S. Rekhi, L. Dubrovinsky, and S. Saxena, High Temp. - High Pressures **31**, 299 (1999).
[34] S. Sinogeikin, J. Bass, V. Prakapenka, D. Lakshtanov, G. Shen, C. Sanchez-Valle, and M. Rivers, Rev. Sci. Instrum. **77**, 103905 (2006).
[35] F. Li, Q. Cui, Z. He, T. Cui, J. Zhang, Q. Zhou, G. Zou, and S. Sasaki, J. Chem. Phys. **123**, 174511 (2005).
[36] H. Shimizu and S. Sasaki, Science **257**, 514 (1992).
[37] C. S. Zha, H. K. Mao, and R. J. Hemley, Proc. Natl. Acad. Sci. U.S.A. **97**, 13494 (2000).
[38] F. Birch, J. Geophys. Res. **83**, 1257 (1978).
[39] S. Fu, J. Yang, and J.-F. Lin, Phys. Rev. Lett. **118**, 036402 (2017).
[40] J. Yang, X. Tong, J.-F. Lin, T. Okuchi, and N. Tomioka, Sci. Rep. **5**, 17188 (2015).
[41] R. Yang and Z. Wu, Earth Planet. Sci. Lett. **404**, 14 (2014).
[42] T. Kume, M. Daimon, S. Sasaki, and H. Shimizu, Phys. Rev. B **57**, 13347 (1998).
[43] A. J. Cohen and R. G. Gordon, Phys. Rev. B **14**, 4593 (1976).
[44] M. Grimsditch, P. Loubeyre, and A. Polian, Phys. Rev. B **33**, 7192 (1986).